

Orbital occupancy and hybridization in strained SrVO₃ epitaxial filmsMathieu Mirjolet^{1,*}, Hari Babu Vasili,² Adrian Valadkhani,³ José Santiso⁴, Vladislav Borisov,⁵ Pierluigi Gargiani,² Manuel Valvidares,² Roser Valentí³, and Josep Fontcuberta¹¹*Institut de Ciència de Materials de Barcelona (ICMAB-CSIC), Campus UAB, Bellaterra 08193, Catalonia, Spain*²*ALBA Synchrotron Light Source, Cerdanyola del Vallès 08290, Catalonia, Spain*³*Institut für Theoretische Physik, Goethe-Universität Frankfurt am Main, 60438 Frankfurt am Main, Germany*⁴*Catalan Institute of Nanoscience and Nanotechnology (ICN2), CSIC, BIST, Campus UAB, Bellaterra 08193, Catalonia, Spain*⁵*Department of Physics and Astronomy, Uppsala University, Box 516, Uppsala SE-75120, Sweden*

(Received 30 March 2021; revised 24 June 2021; accepted 9 August 2021; published 9 September 2021)

Oxygen packaging in transition metal oxides determines the metal-oxygen hybridization and electronic occupation at metal orbitals. Strontium vanadate (SrVO₃), having a single electron in a 3*d* orbital, is thought to be the simplest example of strongly correlated metallic oxides. Here, we determine the effects of epitaxial strain on the electronic properties of SrVO₃ thin films, where the metal-oxide sublattice is corner connected. Using x-ray absorption and x-ray linear dichroism at the V *L*_{2,3} and O *K* edges, it is observed that tensile or compressive epitaxial strain change the hierarchy of orbitals within the *t*_{2*g*} and *e*_g manifolds. Data show a remarkable 2*p*–3*d* hybridization, as well as a strain-induced reordering of the V 3*d*(*t*_{2*g*}, *e*_g) orbitals. The latter is itself accompanied by a consequent change of hybridization that modulates the hybrid *π** and *σ** orbitals and the carrier population at the metal ions, challenging a rigid band picture.

DOI: [10.1103/PhysRevMaterials.5.095002](https://doi.org/10.1103/PhysRevMaterials.5.095002)

I. INTRODUCTION

The interplay between orbital, charge, and spin degrees of freedom in transition metal oxides (TMOs) is at the heart of the myriad of different properties they display, and it is responsible for their extreme responsivity to external stimuli. Electron density (*n*) and conduction bandwidth (*W*) are the knobs that allow fine tuning of the relative strength of these degrees of freedom. TMOs, containing 3*d*^{*n*} cations, have been much explored due to the possibility of tuning and monitoring the strength of electron-electron (*e*-*e*) correlations by increasing *n* or reducing *W*. For instance, in the 3*d*² compound V₂O₃, *e*-*e* correlations open a gap in the 3*d*-derived conduction band upon cooling or under pressure, and the material displays a metal-insulator transition (MIT) from a paramagnetic metal into an antiferromagnetic insulator. Electrical properties of V₂O₃ are thus understood by the presence of a Mott-Hubbard MIT, where correlations are controlled by electronic bandwidth [1,2]. However, at the MIT, there is change of crystal symmetry, and the hierarchy of electronic orbitals, their electronic occupation [3], and their bandwidth [4] change. This implies also changes in hybridization between V 3*d* and O 2*p* orbitals, implying that the electron counting at 3*d*^{*n*} is not preserved, and a simple *d*-orbital Mott-Hubbard description may be insufficient [5]. Similarly, in vanadium dioxide VO₂, changes of the *d*-*p* hybridization in edge-connected oxygen octahedra rule the MIT [4,6]. Not surprisingly, the orbital filling and the MIT of VO₂ have been found to be sensitive to epitaxial strain [7].

In AMO₃ perovskites where the metallic 3*d*^{*n*} ions are within a corner-shared octahedra array, it is well known that lattice deformations by atomic size mismatch, epitaxial strain, etc. rule the hierarchy of 3*d* atomic orbitals. However, the relative changes of metal-oxygen hybridization by epitaxial stress remain rather unexplored. SrVO₃ (SVO) owing to its simple electronic configuration (V⁴⁺, 3*d*¹), its cubic structure, and a relatively broad bandwidth responsible for its high electrical conductivity (with room-temperature resistivity $\rho = 30\text{--}50 \mu\Omega \text{ cm}$) [8,9], has been the *drosophila* for research in correlated systems [10]. Here, we aim to settle if epitaxial strain acting on SVO films could induce a symmetry breaking of the *t*_{2*g*}(*xy*, *xz*, *yz*) orbitals significant enough to modify the 2*p*-3*d* hybridization and the charge distribution within *t*_{2*g*}-2*p* orbitals.

Orbital occupancy can be explored by x-ray absorption spectroscopy (XAS) and particularly by the x-ray linear dichroism (XLD) at the V *L*_{2,3} and O *K* absorption edges. As the XAS intensity is proportional to the available empty states, it would allow us to probe the V 3*d* orbital occupancy as well as the V-O hybridization. Photons with an energy larger than ~ 515 eV can be absorbed at V 2*p*_{3/2} and V 2*p*_{1/2} core levels, and the intensity of the corresponding absorption lines (*L*₃ and *L*₂, respectively) is proportional to the available lowest energy V 3*d* final states (*t*_{2*g*} and *e*_g). Similarly, XAS absorption at the O *K* edge occurs when light is absorbed at O 1*s* core levels and electrons are excited to the lowest energy empty O 2*p* states. Observation of O *K* edge absorption is a fingerprint of the existence of empty states at O 2*p* and thus of the covalence of the V-O bonds. The oxygen O *K* edge occurs at ~ 530 eV, which is only ~ 15 eV above the V *L*₂ edge, and thus, the measured absorption intensity at > 530 eV contains a tail of the V *L*₂ absorption [11].

*mathieu.mirjolet@gmail.com

To get access to the subtle differences in the orbital occupancy of t_{2g} (xy , yz/xz) or e_g (x^2-y^2 , z^2) states, one can collect the x-ray absorption spectra (XAS) for $\mathbf{E}||ab$ and for $\mathbf{E}||c$ (later shortened as \mathbf{E}_{ab} and \mathbf{E}_c , respectively), where ab and c indicate in-plane and out-of-plane x-ray electric field \mathbf{E} directions, respectively. The resulting dichroism [XLD $\approx I(\mathbf{E}_c) - I(\mathbf{E}_{ab})$] is therefore a measure of the difference of empty states at orbitals with in-plane (xy of t_{2g} ; x^2-y^2 of e_g) or out-of-plane (yz/xz of t_{2g} ; z^2 of e_g) symmetries. This technique has been successfully used in recent years to determine orbital occupancy within the different subsets of e_g and t_{2g} orbitals in several TMOs (Ti [12], V, Mn [13,14], Fe, Co [15], Ni [16–18], Cu [19,20], etc.).

Moreover, the O K edge may also display a remarkable *slave* dichroism if the covalently-mixed (p_x, p_y, p_z)- $t_{2g}(xy, xz/yz)$ orbitals and (p_x, p_y, p_z)- $e_g(x^2-y^2, z^2)$ orbitals are differently occupied. Indeed, XLD at the O K edge has been used to unravel electronic reconfigurations in manganite superlattices [21] or the nature of the MIT in VO₂ [22].

Here, aiming at exploring and disentangling the effects of strain and covalency in SVO, films of different thicknesses have been grown on single-crystalline perovskite substrates imposing different epitaxial stresses. The structural and electrical properties of the films have been inspected and their conduction band properties explored by XAS and XLD at $VL_{2,3}$ and O K edges. It turns out that epitaxial strain promotes selective occupancy of V t_{2g} orbitals that, despite the relatively weaker strength of the $\pi^*(t_{2g})$ bonds, also modulates the electron occupancy of hybridized oxygen $2p$ orbitals, where hole occupancy is also affected. Implications of these findings on the understanding of some relevant properties of metallic oxides are discussed.

II. METHODOLOGY

We grew epitaxial [001] textured SVO films on various single-crystalline substrates by pulsed laser deposition at a substrate temperature of 750 °C. It is known that optimal transport properties of SVO films are obtained when growth is performed at the lowest pressure or using a plume-tampering Ar atmosphere [9,23]. Accordingly, we report here on films grown at the base pressure of the growth chamber ($\approx 10^{-7}$ mbar). The number of laser pulses was varied to obtain films with nominal thickness t of 10, 20, and 70 nm, according to the growth rate calibrations. For any given number of laser pulses and pressure conditions, films on different substrates were grown simultaneously to minimize spurious thickness variations. We used single-crystalline substrates with (001) orientation having a (pseudo)cubic lattice parameter either smaller [LaAlO₃ (LAO), $a_S = 3.791$ Å], closely similar [NdGaO₃ (NGO), $a_S = 3.863$ Å], or larger [SrTiO₃ (STO), $a_S = 3.905$ Å] than the cubic cell parameter of bulk SVO ($a_{SVO} = 3.842$ Å). The corresponding mismatch values [$f = (a_S - a_{SVO})/a_S$] are $f(\text{LAO}) = -1.37\%$, $f(\text{NGO}) = +0.52\%$, and $f(\text{STO}) = +1.59\%$. The topography of the film surface was inspected by atomic force microscopy. The surface roughness of the 10 nm films was found to be <0.2 nm ($1 \times 1 \mu\text{m}^2$), slightly increasing up to ~ 0.44 nm when increasing film thickness (see the Supplemental Material [24]). The structural characteristics of the SVO films were

investigated by x-ray diffraction (XRD) using θ - 2θ patterns and reciprocal space maps to determine the out-of-plane (c) and in-plane (a) cell parameters. Electrical resistivity and Hall effect measurements were performed using a PPMS (Quantum Design) under magnetic fields up to ± 9 T.

We measured the XAS spectra of the samples at the V $L_{2,3}$ and O K edges at 300 and 2 K, using horizontally (H) or vertically (V) linearly polarized light, and probed the XLD as the difference between the two light polarizations [see sketch of the measurement configuration in Fig. 4(a)]. The x-ray absorption was collected with V ($\mathbf{E}||ab$, \mathbf{E}_{ab}) and H ($\mathbf{E}||bc$) polarizations, where ab and bc indicate the planes defined by the (a , b , c) crystallographic axes of the sample. For the $3d$ orbitals, the H -polarized XAS spectrum can be different for a grazing incidence ($\mathbf{E}||c$) and the normal incidence ($\mathbf{E}||b$), while the V -polarized spectrum ($\mathbf{E}||a$) remains unchanged except the probing depth. Following the common practice, we collected most of the spectra in the so-called grazing incidence with the x-ray incidence direction \mathbf{k} at an angle $\theta = 30^\circ$ with respect to the sample surface. Henceforth, we label the electric field vectors \mathbf{E}_c and \mathbf{E}_{ab} for the H - and V -polarized lights, respectively. The XAS-generated photocurrent was measured in the total electron yield (TEY) mode. XAS data in TEY mode could be robustly collected from 300 to 2 K, confirming the metallic nature of the SVO films in this temperature range. Average XAS spectra were obtained by averaging the XAS intensities collected for both linear polarizations, i.e., $\text{XAS} = [I(\mathbf{E}_c) + I(\mathbf{E}_{ab})]/2$. The XLD signal is defined as $\text{XLD} = I(\mathbf{E}_c) - I(\mathbf{E}_{ab})$. All XAS/XLD experiments were performed at BL29 BOREAS beamline of ALBA synchrotron, Catalonia, Spain [25].

The electronic properties of SrVO₃ were calculated using density functional theory (DFT) within the generalized gradient approximation, as available in the all-electron full-potential localized orbitals basis set code [26,27], and the generalized gradient approximation as exchange-correlation functional [28]. The integration in the Brillouin zone was performed using the trapezoidal method and a $(20 \times 20 \times 20)$ \mathbf{k} -mesh, in the -10 to 0 eV (corresponding to E_F) interval. The contributions of different orbitals to the density of states was determined based on the Wannier analysis which includes the vanadium $3d$ and oxygen $2p$ states around the Fermi level. The lattice parameters were taken from our measurements of SrVO₃ (10 nm) films grown on different substrates.

III. RESULTS

Illustrative XRD data for SVO (10 nm) films on different substrates are shown in Fig. 1(a) (data for all films are shown in the Supplemental Material [24]). Laue fringes in the θ - 2θ patterns are very well visible, assessing the film quality, and allowing us to confirm the film thickness determined from the growth rate and to extract the out-of-plane lattice parameters (c axis) by simulating the XRD pattern. From the fitting of θ - 2θ scans and the analysis of the reciprocal space maps, we deduced the cell parameters (a , c) and the tetragonality ratio c/a shown in Fig. 1(b). Dedicated reciprocal space maps were also collected to assess the absence of octahedral tilting or rotations (see the Supplemental Material [24]). It is observed

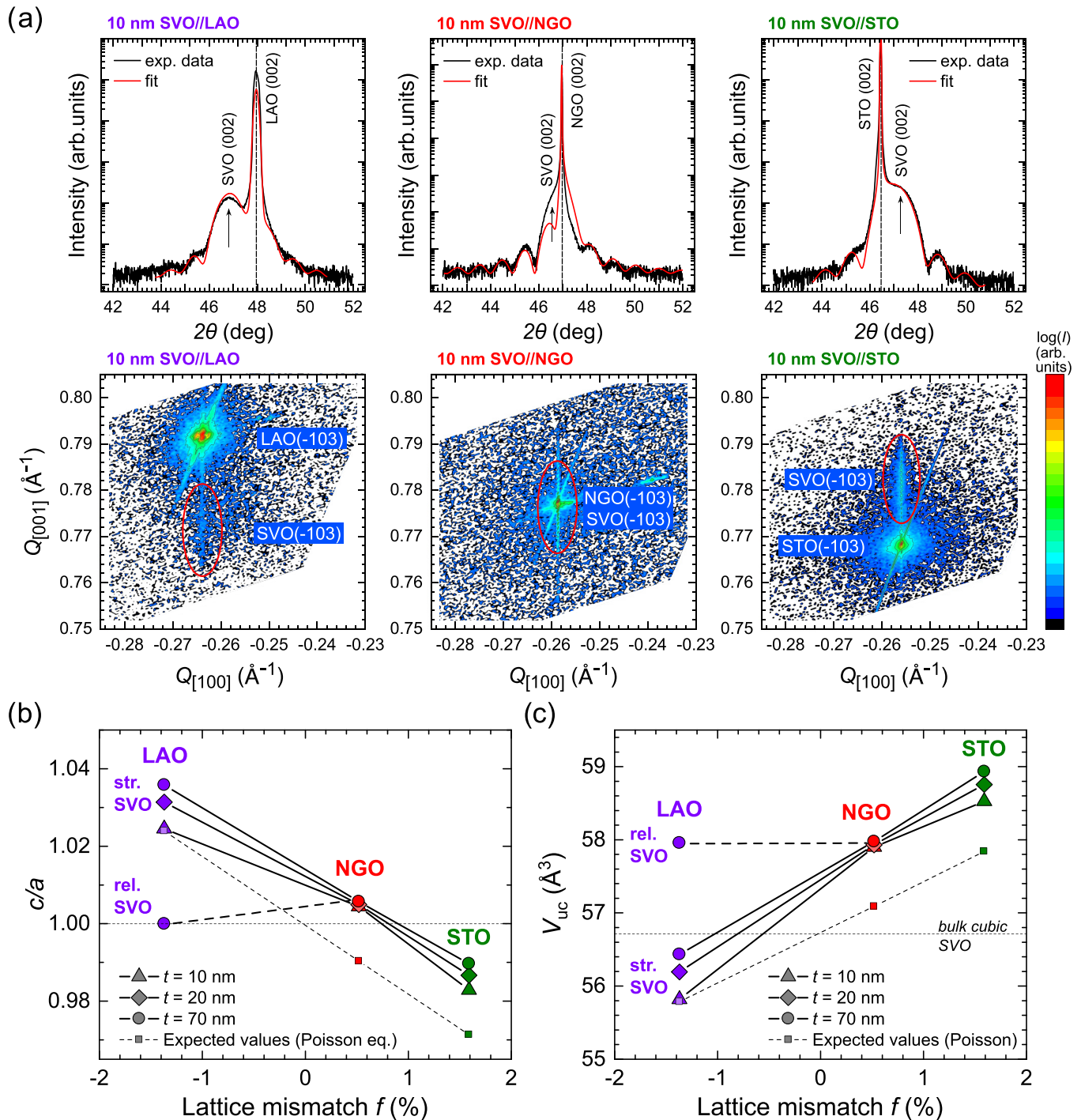


FIG. 1. (a) Top panel: θ - 2θ scans of SVO films of $t = 10$ nm, on STO, NGO, and LAO substrates. The continuous red lines are the results of the optimal simulation used to extract the c axis and the film thickness. Bottom panel: The corresponding reciprocal space maps measured around the (-103) reflection. The SVO reflection is circled. (b) Experimental c/a ratio for SVO films of various thicknesses (10, 20, and 70 nm), grown on LAO, NGO, and STO substrates. The dashed line indicates the expected c/a values for fully strained films ($a = a_s$), and c is calculated using the Poisson equation (with Poisson ratio $\nu = 0.28$). (c) Measured unit cell volume V_{uc} as a function of structural mismatch f . The dashed line indicates the unit cell volume calculated using the indicated Poisson ratio. Dotted lines in (b) and (c) indicate the c/a ratio and unit cell volume of cubic bulk SVO, respectively.

that all films, except the 70 nm on LAO, have the in-plane cell parameters (a axis) coinciding with those of substrates, and thus, these films are coherently strained on the corresponding substrates (Figs. 1(a) and S2 in the Supplemental Material [24]). In contrast, the reciprocal space map of the (70-nm-

thick) SVO/LAO film reveals the coexistence of fully strained and partially relaxed regions (Fig. S2 in the Supplemental Material [24]).

Figure 1(b) depicts the tetragonality ratio c/a for all films evaluated from the extracted (a , c) cell parameters. It can

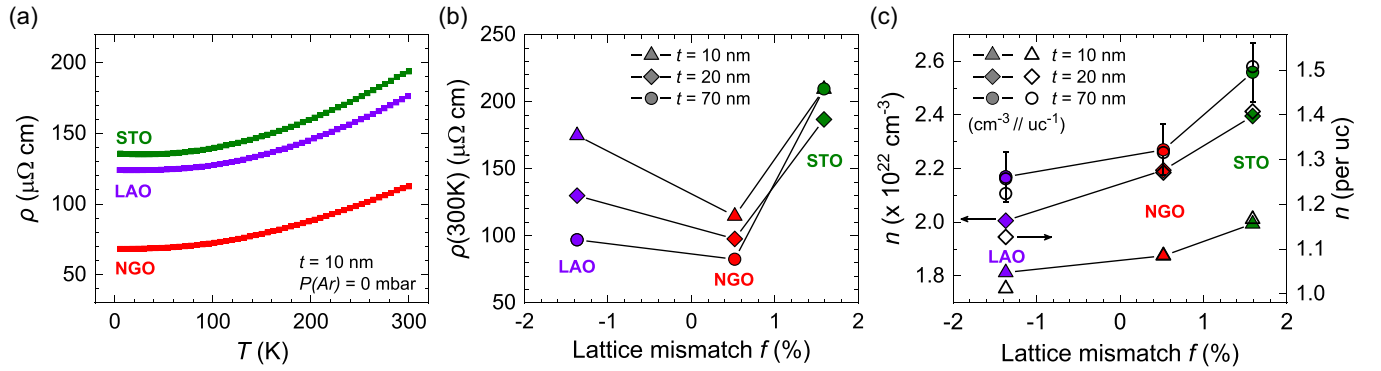


FIG. 2. (a) Temperature dependence of the resistivity of SVO (10 nm) films grown on various substrates. (b) Dependence of the room-temperature resistivity of films of 10, 20, and 70 nm grown on substrates having different lattice mismatch (f) as indicated. (c) Carrier concentration (n) per unit volume of film (cm^{-3} ; left axis) and per unit cell (right axis). Error bars (shown only for the 10 nm series for the sake of clarity) are calculated assuming a maximum error of 5% in thickness determination and neglecting any possible contribution from the substrate.

be appreciated that the tetragonality increases from STO to NGO and to LAO. For SVO//STO films, $0.98 \leq c/a \leq 0.99$ (depending on thickness) would indicate a tensile stress compared with cubic SVO, whereas the SVO//LAO films, having $1.025 \leq c/a \leq 1.035$, would be consistent with a compressive stress. SVO//NGO films are marginally tensile stressed ($1.004 \leq c/a \leq 1.006$). Overall, this is the expected structural response of a SVO film to the tensile-to-compressive film/substrate mismatch. We also include in Fig. 1(b) (solid squares, dashed line) the predicted tetragonality ratio of SVO//STO, SVO//NGO, and SVO//LAO films calculated using the reported Poisson ratio for SVO ($\nu \approx 0.28$) [29] to account for the elastic response of the SVO lattice to in-plane epitaxial strain (ϵ). For coherently grown films, $\epsilon = f$. It can be appreciated that the measured c/a values of strained films display the expected dependence on epitaxial strain. However, the values of c/a are found to be larger than the ones predicted using the Poisson ratio, which suggests an expansion of the c axis that cannot be explained exclusively by an elastic deformation of the lattice. Observation of an anomalous expansion of the out-of-plane c axis in epitaxial oxide thin films, more noticeable in films on STO and NGO imposing a tensile strain, is a common finding and typically attributed to oxygen defects in the lattice, which are predicted to be more abundant in films under tensile strain [30]. Consistent with the observed partial relaxation of the compressively stressed SVO//LAO, the experimental c/a values of the relaxed fraction of the film falls below the extrapolated fully strained c/a values. As shown in Fig. 1(c), the measured unit cell volume (V_{uc}) of SVO films under tensile strain is larger than that of bulk SVO. There is a clear expansion of the unit cell with increasing tensile strain (i.e., reducing c/a), which indicates that point defect incorporation depends on strain being more pronounced for tensile strain than for the compressive one [30].

All SVO films reported here, including the thinnest ones ($t = 10$ nm), are metallic (Fig. 2(a) and the Supplemental Material [24]) with residual resistivity ratios [RRR = $\rho(300\text{K})/\rho(5\text{K})$] ranging from 1.4 to 1.7 for the thinnest films (10 nm) and increasing to 1.6–2.1 for the thicker films (70 nm). In agreement with previous findings, the largest RRR is obtained in films on the best matching substrate

(NGO) [31]. As shown in Fig. 2(b), the resistivity of the films slightly decreases upon increasing thickness. In Fig. 2(c), we show the carrier density (n) per unit volume ($1/\text{cm}^3$; left axis) as extracted from room-temperature Hall measurements. Carrier density values are in the $(1.8\text{--}2.6) \times 10^{22} \text{ cm}^{-3}$ range, which is within the range of reported values for similar SVO films: $2.26 \times 10^{22} \text{ cm}^{-3}$ [8] and $(2.0\text{--}2.3) \times 10^{22} \text{ cm}^{-3}$ [32]. It is worth noticing that SVO films of similar thickness grown under the same nominal conditions, on LSAT and NGO, both substrates having similar mismatch, have also similar carrier concentration ($2.14 \times 10^{22} \text{ cm}^{-3}$) [9,31]. It can be appreciated in Fig. 2(c) that n increases when increasing the tensile strain. This observation agrees with the observed expansion of the unit cell and the possible role of nonstoichiometric defects on this remarkable trend.

In Fig. 3(a), we show the average XAS of 10 nm SVO films recorded at grazing incidence on LAO, NGO, and STO substrates in the energy range of 510–555 eV, where the $V L_{2,3}$ absorption edge is present and followed by the O K edge. The $V L_3$ (~ 519 eV) and $V L_2$ (~ 525.5 eV) edges are very visible, but the O K edge prepeak has a slight overlap with the $V L_2$ edge and extends to a wide energy region (530–550 eV). The $V L_{2,3}$ edge is expected to differ for different valence states of V^{m+} ions (e.g., V^{3+} , V^{4+} , V^{5+}), lowering in energy upon reducing of the valence state, and its shape is further enriched by the presence of multiplet fine structure whose contribution largely depends on the local symmetry and the electron density [33,34]. The chemical shifts in the XAS $L_{2,3}$ spectra of Fig. 3(a) are consistent with the $V 3d^1$ electronic configuration. The $V 3d^2$ systems display a characteristic splitting at $V L_2$ line [34], and V^{5+} systems have a distinctive peak at 515 eV [35] which are both absent in our spectra. Moreover, the overall shape of the XAS spectra closely resembles that predicted for SrVO_3 [36] and it is extremely similar to that reported for isoelectronic CaVO_3 [37]. It follows that, within the depth probing sensitivity (≈ 5 nm) of XAS in TEY mode, V^{4+} ($3d^1$) is the dominant formal state of the transition metal in our 10 nm SVO films. It is worth noticing that the positions of the $L_{2,3}$ peaks are preserved irrespectively on the substrate. This indicates that changes of valence state of V^{4+} due to epitaxial strain, if any, are beyond

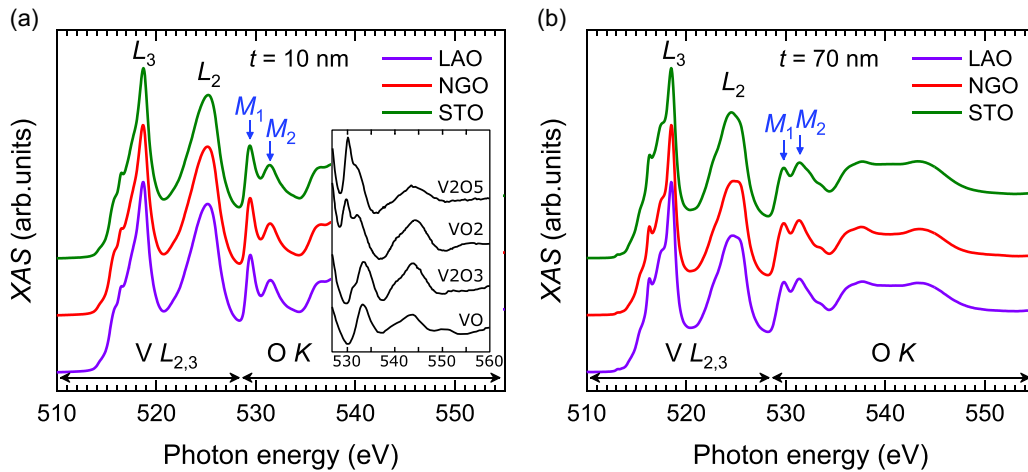


FIG. 3. X-ray absorption spectroscopy (XAS) of $V L_{2,3}$ and $O K$ absorption edges recorded at room temperature of SVO films grown on STO, NGO, and LAO, and for thicknesses of (a) 10 nm and (b) 70 nm. The energy ranges of $V L_{2,3}$ and $O K$ edges are indicated along the x axis. Arrows of M_1 and M_2 at $O K$ edge prepeak doublet represent the main absorption lines between $O 1s$ and $O 2p$ states, hybridized with $3d-t_{2g}$ and $3d-e_g$ states. Inset in (a): Illustrative $O K$ XAS data for different VO_x oxides (experimental data adapted from Hébert *et al.* [38]).

experimental resolution. The XAS at $L_{2,3}$ edges of the 70 nm SVO films [Fig. 3(b)] does not allow us to appreciate any shift depending on the substrate. Expanded energy scale analysis, however, indicates that the $L_{2,3}$ edges of the 70 nm films are shifted by ~ 0.3 eV toward lower energy compared with the

10 nm films [Figs. 4(b) and 4(c)]. In the common rigid band picture, this would imply that V^{m+} ions in the 70 nm films are somewhat reduced, say $V^{(4-\delta)+}$ ($\delta = 0.15-0.2$), compared with the 10 nm films. This observation is in agreement with the observed slight expansion of the unit cell volume and the

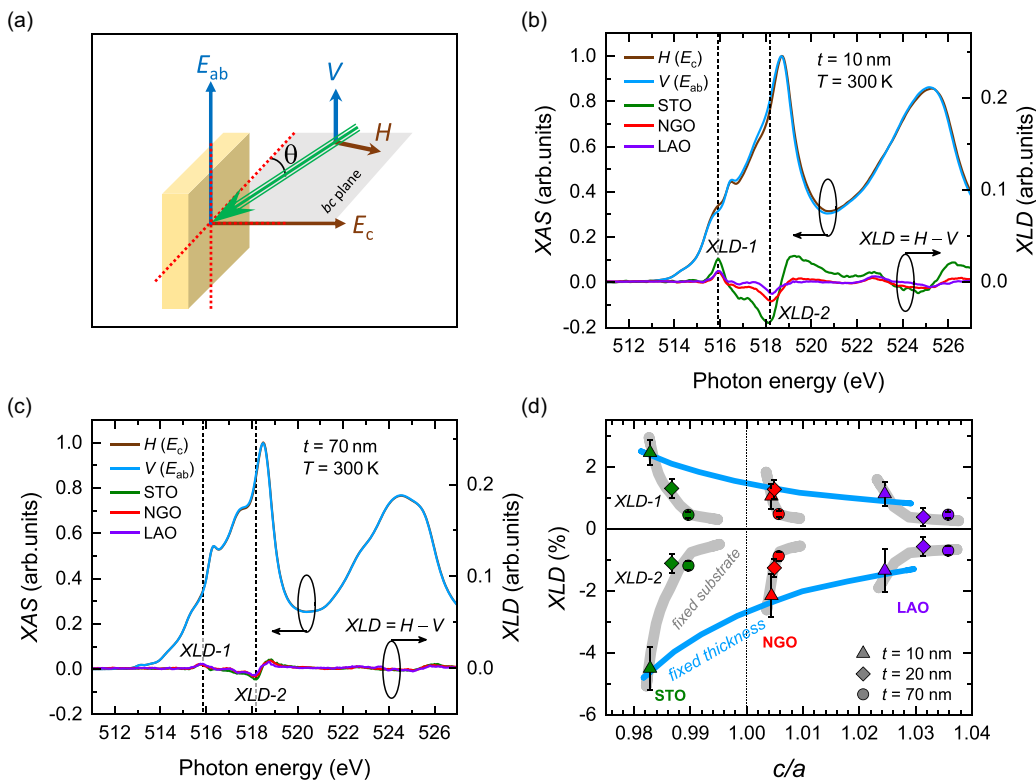


FIG. 4. (a) Experimental arrangement for x-ray absorption spectroscopy (XAS) and x-ray linear dichroism (XLD) measurements. (b) and (c) Illustrative H - and V -polarized XAS spectra (collected at room temperature and grazing incidence $\theta = 30^\circ$) of 10 and 70 nm SVO//STO film, respectively. Bottom spectra of the panels represent the XLD spectra [i.e., $I(E_c) - I(E_{ab})$] for each substrate (STO, NGO, and LAO). Some reference energies, XLD-1 and XLD-2, for maxima of positive and negative dichroism, respectively, are indicated by vertical dashed lines. (d) Summary of the XLD maxima values of SVO films for various thicknesses (10, 20, and 70 nm) grown on STO, NGO, and LAO substrates.

carrier density variation when increasing thickness observed in strained films [Figs. 1(c) and 2(c), respectively].

We now focus our attention on the XAS at the O *K* edge, associated with transitions between O *1s* and O *2p* orbitals, and particularly to the prepeak doublet maxima appearing at M_1 (~ 529.5 eV) and M_2 (~ 531.5 eV) indicated by arrows in Figs. 3(a) and 3(b), which are known to be sensitive to oxygen contents [38,39]. The very presence of the M_1 and M_2 peaks indicates that empty final states are available at O *2p* orbitals. This doublet is a fingerprint for the hybridization between O *2p* and metal $3d - t_{2g}$ and between O *2p* and $3d - e_g$ states, respectively. Correspondingly, the energy difference $\Delta M = M_2 - M_1 \approx 2$ eV is a measure of the so-called *ligand field energy splitting* $\Delta E = E(e_g) - E(t_{2g})$ [38,40]. The relative intensity $I[M_1(t_{2g})]/I[M_2(e_g)]$ is sensitive to the electronic occupancy at V *3d* levels, which should vary according to the valence state of V^{m+} ions and hybridization. We note that an accurate determination of this ratio is challenged by the presence of the tail of the vanadium L_2 edge; therefore, we will restrict ourselves to a qualitative analysis. For the $t = 10$ nm SVO films of Fig. 3(a), the $I(M_1)/I(M_2)$ ratio is in excellent agreement with reference data for VO_2 oxide [as reproduced in the inset of Fig. 3(a)] [38,41]. Therefore, the $I(M_1)/I(M_2)$ ratio closely matches that reported for an average $V d^1$ configuration, without perceptible changes when changing the substrates. Liberati *et al.* [37], reporting XAS of $CaVO_3$ films grown on different substrates, obtained similar spectra to those of Fig. 3(a) and concluded that V^{4+} (d^1) oxidation state was prevalent in all films. It is worth noticing that comparison of the XAS O *K* spectra recorded at normal and grazing incidence do not reveal any discernible chemical shift—within the experimental resolution (< 10 meV)—suggesting that, within the sensitive penetration depth, the SVO films are electronically homogeneous (see the Supplemental Material [24]).

The O *K* edge of the $t = 70$ nm films on various substrates [Fig. 3(b)] shows a reduction of the $I(M_1)/I(M_2)$ ratio, indicating that the density of *2p* final states has changed due to strain-related modification of hybridization and/or a change of the number of electrons [38]. Indeed, if the formal charge of V^{4+} would reduce to V^{3+} , implying a higher density of electrons mostly at $2p - t_{2g}$ orbitals, then the available holes at *2p* hybrids would decrease, and correspondingly, the M_1 intensity would be reduced. Consistently, the Hall effect data [Fig. 2(c)] signal an increase of carrier density of ~ 22 – 25% . A consistent increase of c/a with thickness is observed for films on LAO and STO, while thickness does not modify appreciably c/a in NGO [Fig. 1(c)]. As films on all substrates display a similar modification of the $I(M_1)/I(M_2)$ ratio, we conclude that carrier density seems to contribute to the apparent differences in O *K* XAS when changing film thickness, while it is reflected as a minor shift in V $L_{2,3}$ XAS, as mentioned above.

We next aim at addressing if the electron distribution within the $3d(t_{2g}, e_g)$ manifold is affected by substrate mismatch and film thickness. The XAS data in Figs. 3(a) and 3(b) give a first hint. Indeed, the fine structure of the V L_3 edge is related to final states available at t_{2g} and e_g orbitals. XAS features at the lower energy side of the L_3 edge were assigned to xy and xz/yz orbitals [42]. Recently, Wu *et al.* [36] used a configuration interaction approach to calculate XAS for V^{4+} in octahedral coordination and noticed that

these multiplet-related features are very sensitive to tetragonal deformations of the coordination VO_6 polyhedra. The shape of L_3 in our spectra [Figs. 3(a) and 3(b)] closely resembles those calculated for strained SVO films [36]; however, raw V L_3 XAS data do not allow us to obtain a deeper insight into electron occupancy and its dependence on substrate.

Therefore, we turn now to exploit the sensitivity of XAS to the polarization direction of the incoming photons to deduce XLD and to identify the symmetry of occupied states. As already mentioned in the experimental section, the data were collected for the light incidence direction \mathbf{k} at an angle θ with the sample surface, with the electric field vector pointing along two perpendicular directions: V ($\mathbf{E}||ab$) and H ($\mathbf{E}||bc$), where ab and bc indicate the planes defined by the (a , b , c) crystallographic axes of the sample. In these polarization-dependent experiments, the spectra were collected at various θ angles (8° , 30° , 60° , and 85°) with respect to the film surface (b axis) from nearly in-plane (8°) to almost normal incidence (85°). At $\theta = 0^\circ$, the electric field \mathbf{E} of H -polarized light is perpendicular to the sample surface, along the c axis (and $\mathbf{E} = \mathbf{E}_c$), whereas at $\theta = 90^\circ$, \mathbf{E} is parallel to it, along the b axis ($\mathbf{E} = \mathbf{E}_b$).

Aetukuri *et al.* [7] showed that an insight into orbital occupation in V^{4+} can be safely achieved by restricting the XLD analysis to the lowest-energy excitonic part of the V L_3 spectra (512–516 eV, range). On the other hand, extraction of V *3d* related XLD values requires appropriate normalization of the raw XAS spectra collected for H and V polarizations. A partial overlapping between the V L_2 postedge and O *K* edge prepeak is known to be an issue for V *L* edge spectroscopy, and background subtraction is prone to introduce errors in quantitative analyses [34]. Therefore, we restrict ourselves to the excitonic region, and we have normalized the spectra to ~ 528 eV, just at the L_2 postedge to minimize the impact of the O *K* edge to the absorption. The spectra were further normalized to the average intensity of the V L_3 peak to allow the quantitative data analysis of the V L_3 XLD peak.

In Fig. 4(b), we show XAS at the V $L_{2,3}$ edges of 10-nm-thick SVO films grown on various substrates (STO, NGO, and LAO) recorded at room temperature and $\theta = 30^\circ$, implying that the \mathbf{E} of V -polarized spectra is parallel to the sample surface (\mathbf{E}_a , commonly written as \mathbf{E}_{ab}), and the \mathbf{E} of H -polarized spectra is almost perpendicular to it (\mathbf{E}_c) [Fig. 4(a)]. Notable differences can be observed in the raw V L_3 XAS intensities, but they are better appreciated in the corresponding dichroic XLD signals shown in the bottom part of Fig. 4(b). Two different energies at V L_3 XLD signals are selected for the discussion, indicated by dashed vertical lines and labeled as XLD-1 and XLD-2, where XLD displays well-defined maxima for positive and negative dichroism. It is apparent that the amplitudes of the corresponding XLD-1 and XLD-2 intensities are largest for the SVO films on STO but reduce for the films on NGO and LAO. Data recorded at 2 K display a very similar trend (see the Supplemental Material [24]). XLD measurements have been done on the SVO films of 20 and 70 nm thicknesses in a similar manner. For instance, in Fig. 4(c), we show the data for 70 nm SVO films (data for the 20 nm films are in the Supplemental Material [24]). It can be appreciated that the XLD displays similar features as in the 10 nm films [Fig. 4(b)], except that the

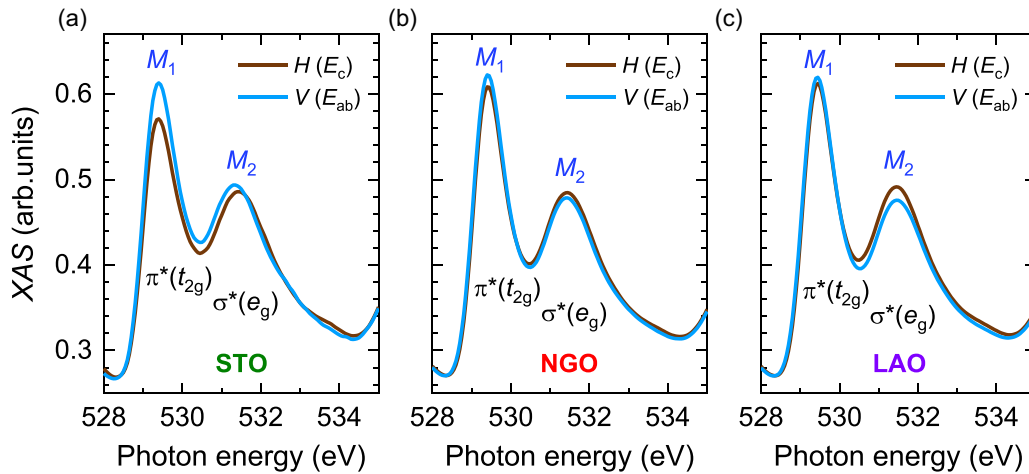


FIG. 5. O K edge x-ray absorption spectroscopy (XAS) prepeak of 10 nm SVO films grown on (a) STO, (b) NGO, and (c) LAO. A significantly larger dichroism at t_{2g} peak for STO than for NGO/LAO and the reverse at e_g peak reflect changes of hybridization with strain. Data were recorded at room temperature.

amplitudes at XLD-1 and XLD-2 are reduced with the increasing thickness. Figure 4(d) summarizes the XLD maxima values by displaying the amplitudes of XLD-1 and XLD-2 for each substrate (STO, NGO, and LAO) with different thicknesses (10, 20, and 70 nm), both parametrized by the corresponding c/a tetragonality ratio. Data show two main trends. First, the magnitude of XLD-1 and XLD-2 decreases from STO to LAO substrates, most noticeable in the thinnest films. Second, data also evidence that, upon increasing film thickness and reducing the octahedral distortion $|1-c/a|$, XLD progressively lowers, the effect being more remarkable in the most strained films (SVO//STO) and weaker in the partially relaxed films (SVO//LAO). Therefore, data in Fig. 4(d) provide an insight on the impact of substrate and thickness on orbital occupancy in SVO films.

Figure 4(d) also contains XLD data of the 20 and 70 nm SVO films on different substrates. The same trend as in the thinnest films can be observed, with the amplitude of the XLD signal at XLD-1 reducing when increasing thickness. However, we noticed above that, in thicker films, the XAS data at the O K edge and Hall data suggest some V^{4+} reduction to V^{3+} that could signal a decrease in the oxygen contents in the film, thus changing not only the electronic distribution within the $3d$ orbitals but also its density.

Therefore, we concentrate in the following on the data of the thinnest SVO (10 nm) films, where no traces of charge modification could be identified in XAS at $VL_{2,3}$ and O K edges, on the search for a more robust evidence of changing electron occupancy with substrate-induced stress. The XLD at the XLD-2 feature has its sign reversed ($XLD < 0$) with respect to XLD-1 and displays a mirror dependence on the tetragonality ratio c/a and on film thickness. The presence of XLD features (XLD-1 and XLD-2) of opposite sign differing by ~ 2.2 eV is fully consistent with calculations by Wu *et al.* [36].

We next focus on the sign of the dichroic signal. To minimize multiplet-configuration mixing effects [36,42,43], we restrict ourselves to the dichroic signal observed at the lowest energy range. In Fig. 4(d), it is apparent that the

dichroic signal at XLD-1 is positive, implying that the XAS intensity recorded with \mathbf{E}_{ab} is smaller than the \mathbf{E}_c . In the simplest electron-hole picture, this would indicate that xy orbitals are more occupied than xz/yz . Data show that this orbital polarization is gradually reduced from STO to NGO to LAO, although XLD (XLD-1) remains positive for all films ($t = 10$ nm). Accordingly, the xy orbitals are most favorably occupied in all films, irrespectively of $c/a > 1$ or $c/a < 1$. XLD measurements were recorded at different angles (8° , 30° , 60° , and 85°) for the thinnest films (10 nm), confirming the systematic variation of the XLD signal with substrate (see the Supplemental Material [24]).

As mentioned, electronic occupancy at metal t_{2g} orbitals should have its fingerprint on the O K edge XAS and the XLD at the O K edge. Accordingly, XLD data at the O K edge has been determined as for $VL_{2,3}$. In Fig. 5, we show the XAS spectra in the O K region of 10 nm SVO films grown on the different substrates, collected at the grazing incidence ($\theta = 30^\circ$) with the \mathbf{E}_c and \mathbf{E}_{ab} polarizations as indicated.

To analyze the XAS data in Fig. 5, we recall that the M_1 and M_2 peaks correspond to available states at O $2p$ orbitals hybridized with ligand field split $V 3d$ states, resulting in $\pi^*(t_{2g})$ and $\sigma^*(e_g)$ orbitals. The intensity of the $\pi^*(t_{2g})$ absorption peak is considerably larger than the one of the $\sigma^*(e_g)$ peak: $I[\pi^*(t_{2g})]/I[\sigma^*(e_g)] \approx 1.25$ (Fig. 6, right axis). This difference originates from the larger multiplicity of the t_{2g} orbitals than e_g ones ($\frac{3}{2} = 1.5$) modulated by the distinct hybridization of $\pi^*(t_{2g})$ and $\sigma^*(e_g)$ orbitals. It can be also appreciated in Fig. 5 that the energy difference between $\Delta E_{CF} = E[\sigma^*(e_g)] - E[\pi^*(t_{2g})]$ is of ~ 2.0 eV, as commonly found for early TMOs [40,44], and virtually insensitive to the substrate. Next, we focus on the O K XLD signal defined as the XAS intensity at the corresponding $I[\pi^*(t_{2g})]$ and $I[\sigma^*(e_g)]$ maxima recorded using $I(\mathbf{E}_{ab})$ and $I(\mathbf{E}_c)$ [$XLD = I(\mathbf{E}_c) - I(\mathbf{E}_{ab})$]. In Fig. 6 (left axis), we show the XLD values for films on various substrates.

It is clear in Fig. 6 [and data in Fig. 5(a)] that, for the tensile-strained SVO//STO film (smallest c/a ratio), the XAS intensity $I[\pi^*(t_{2g})]$ is larger for \mathbf{E}_{ab} than for \mathbf{E}_c ,

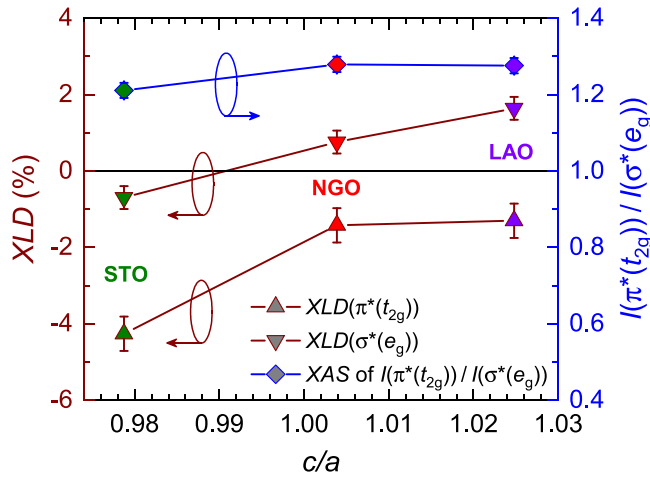


FIG. 6. Left axis: X-ray linear dichroism (XLD) at O K edge for SVO films (10 nm thick) on substrates imposing different tetragonality ratios (c/a). Square symbols indicate the XLD at $\pi^*(t_{2g})$ and $\sigma^*(e_g)$ absorption peaks, as indicated. Right axis: $I[\pi^*(t_{2g})]/I[\sigma^*(e_g)]$ intensity ratios. Data were recorded at room temperature.

and accordingly, $XLD[\pi^*(t_{2g})] < 0$. The observation that $XLD[\pi^*(t_{2g})] < 0$ indicates a higher concentration of holes at $(p_x + p_y)$ orbitals of the $(p_x + p_y) - d_{xy}$ hybrid. In other words, strain modifies the $\pi^*(t_{2g})$ p - d hybridization, driving charge (for $c/a < 1$) from the $p_x + p_y$ orbitals toward the metal. Analogous reasoning accounts for the observed reduction of $XLD[\pi^*(t_{2g})]$ when increasing c/a . Similarly, the dependence of $XLD[\sigma^*(e_g)]$ on c/a also reflects the corresponding changes of $\sigma^*(e_g)$ hybridization.

These observations can be rationalized based on strain modification of $2p$ - $3d$ hybridization and subsequent changes in the electron occupancy at $2p$ - $3d$ hybridized orbitals. We notice that, in an octahedral VO_6 environment, symmetry

arguments dictate that, focusing on the VO_2 plane of the SVO structure, d_{xy} hybridizes with $(p_x + p_y)$, d_{xz} hybridizes with $(p_x + p_z)$, and d_{yz} hybridizes with $(p_y + p_z)$, whereas $d_{x^2-y^2}$ hybridizes with $(p_x + p_y)$ and d_{z^2} with p_z , as illustrated in the Fig. 7 (central panel) and Figs. 7(a) and 7(b).

Under tensile strain (SVO//STO), d_{xy} orbitals are pushed down, as observed by $XLD(V L_{2,3})$. Consequently, the hybridized orbital is shifted down [Fig. 7(a)], and the (p_x, p_y) orbitals which are hybridized with d_{xy} are electron depleted by charge transfer to the metal. Accordingly, XAS at the O K edge should be larger for E_{ab} (more holes available) than for E_c , and thus, $XLD[\pi^*(t_{2g})]$ should be negative (< 0), as we observed. Similarly, when SVO films are under compressive stress (SVO//LAO), $d_{xz,yz}$ orbitals are shifted down in energy, as observed by $XLD(V L_{2,3})$. Therefore, the hybridization of these orbitals with the corresponding p_z orbitals [Fig. 7(b)] implies that the p_z orbitals are electron depleted (hole rich), and correspondingly, $XLD[\sigma^*(e_g)]$ is positive (> 0), as we experimentally observed (Fig. 6).

To analyze the role of tetragonal distortion on the electronic structure of SVO, we performed first-principles DFT calculations. Of interest here is the integrated partial density of states (IDOS) associated with oxygen (p_x, p_y, p_z) and vanadium $3d(t_{2g}, e_g)$ orbitals and to disclose how their relative weight evolve with c/a .

In Fig. 8(a), we show the sum of the IDOS of in-plane (x^2-y^2, xy) and out-of-plane (z^2, xz, yz) orbitals of $3d-e_g$ and $3d-t_{2g}$ manifolds as a function of the tetragonal distortion c/a determined in SVO films on STO, NGO, and LAO ($c/a = 0.978, 1.003, 1.024$, respectively). We also include in Fig. 8(a) the data for a cubic SVO of cell parameter $a = c = 3.86 \text{ \AA}$, corresponding to the unit cell parameter of an unstrained cubic SVO film of volume 57.5 \AA^3 [Fig. 1(c)]. IDOS plots for every individual orbital are included in the Supplemental Material [24]. Data in Fig. 8(a) clearly show that in-plane orbitals are stabilized under tensile strain ($c/a < 1$);

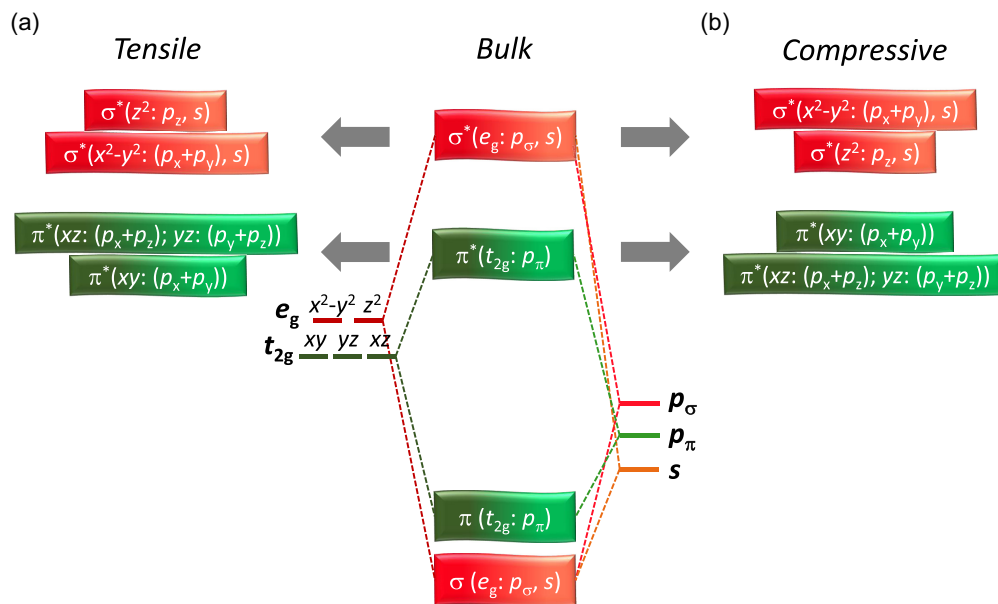


FIG. 7. Central panel: Energy-band diagram for $SrVO_3$ thin films. The hybridized (σ, σ^*) and (π, π^*) orbitals and their parentage are indicated. The symmetry broken hybridized orbitals under the effect of (a) tensile strain and (b) compressive strain.

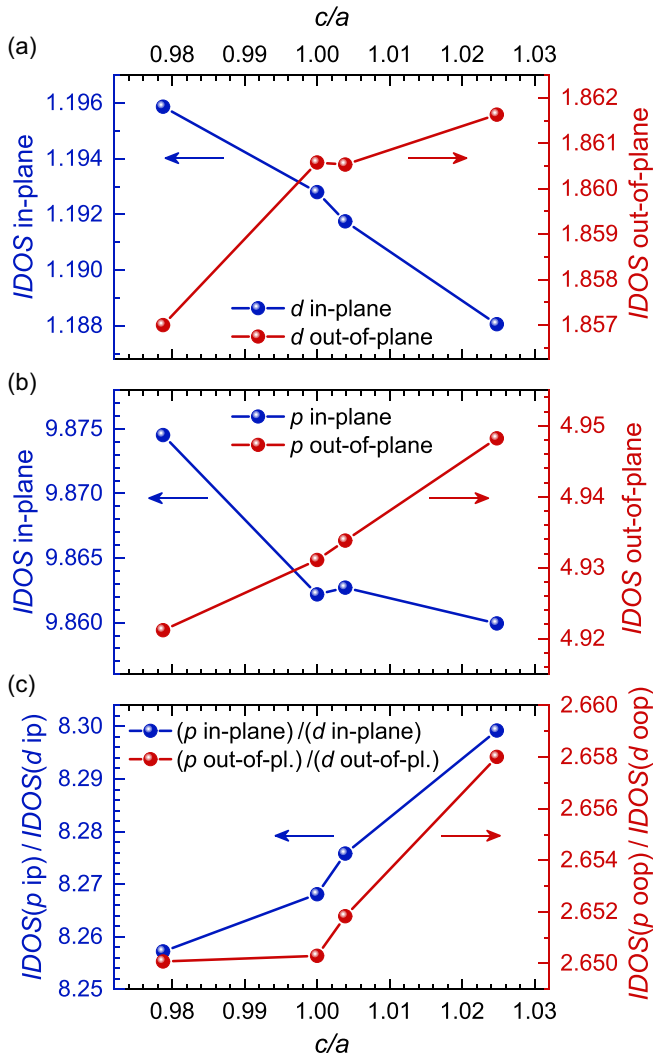


FIG. 8. (a) Sum of the integrated partial density of states (IDOS) of in-plane (left axis) and out-of-plane (right axis) $3d$ orbitals. (b) Similar data for in-plane (left axis) and out-of-plane (right axis) $2p$ orbitals. (c) Ratio between the total density of states of $2p$ and $3d$ character IDOS($2p$)/IDOS($3d$) in-plane (left) and out-of-plane (right).

the opposite trend is observed for out-of-plane orbitals. This agrees with data in Fig. 4(d). The same trend can be appreciated in Fig. 8(b), where we show IDOS of in-plane and out-of-plane $2p$ orbitals. Therefore, p - d hybridized in-plane orbitals move in unison under tetragonal cell distortion and similarly do the out-of-plane hybridized orbitals. However, the relative p/d relative weight in hybrid orbitals is not preserved when changing c/a , as clearly indicated by data in Fig. 8(c), where the IDOS ratios [IDOS(p)/IDOS(d)] for in-plane (left) and out-of-plane (right) orbitals are depicted (see also the Supplemental Material [24]). This implies a charge redistribution among V-O bonds under strain. Indeed, the $2p$ orbitals become progressively more occupied when increasing c/a . Oppositely, for $c/a < 1$, the ratio [IDOS(p , in-plane)/IDOS(d , in-plane)] lowers compared with its value for $c/a = 1$. This implies that the in-plane orbitals of $3d$ character are pushed down compared with the corresponding hybridized $2p$ orbitals, which thus have a relatively lower IDOS, as

argued above (charge balancing sketches are shown in the Supplemental Material [24]). Correspondingly, the available states at $2p$ in-plane orbitals become larger. This accounts for the observed XLD[$\pi^*(t_{2g})$] < 0 observed for $c/a < 1$, as shown in Fig. 6. Similar reasoning accounts for the observed XLD variation for $c/a > 1$.

IV. SUMMARY AND CONCLUSIONS

In summary, bulk SrVO₃ is cubic, but when SVO films are grown on substrates having different structural mismatch with SVO, epitaxial growth imposes compressive or tensile strain on the film structure, and its tetragonality ratio can be varied from $c/a > 1$ to $c/a < 1$ depending on the substrate used and the film thickness. XAS at V $L_{2,3}$ and O K edges of the thinnest films (10 nm) display almost identical features fully consistent with the expected $3d^1$ V⁴⁺ electronic configuration of this oxide. XLD is very well visible at $L_{2,3}$ edges, indicating that the $3d$ - t_{2g} orbitals are not degenerate but signaling a clear hierarchy of (xy , xz , yz) orbitals that gradually varies with the epitaxial strain. In films having an in-plane tensile strain (SVO//STO), the in-plane xy orbitals are preferentially occupied by electrons, gradually leveling out in films under compressive strain. XAS at the O K edge provides clear evidence of a relevant $2p$ - $3d$ hybridization. XLD at the O K edge indicates that hybrid π^* orbitals in epitaxially tensile strained films having an in-plane symmetry have a hole density that decreases in compressive strained films. The consistent variation of occupancy in $2p$ and $3d$ orbitals with strain shows that substrate-induced symmetry breaking modulates orbital occupancy at the metal site but also the metal-oxygen hybridization. It follows that charge density at the metal site is not preserved under strain but redistributes within the hybridized bonds. However, whereas in the case of edge-shared coordination polyhedral (VO₂ case), changes of hybridization with temperature or strain are strong enough to promote a MIT, in the corner-connected octahedral networks, strain slightly modifies the electrical conductivity, but SVO films (at least ≥ 10 nm) remain metallic. Still, the rigid band image of an electron redistribution restricted within the $3d$ - t_{2g} manifold and dictated by strain does not hold in the simplest $3d^1$ perovskite with corner-sharing octahedral network, but hybridization plays a relevant role.

ACKNOWLEDGMENTS

Financial support from the Spanish Ministry of Science, Innovation and Universities, through the ‘‘Severo Ochoa’’ Programme for Centres of Excellence in R&D (FUNFUTURE, CEX2019-000917-S) and the MAT2017-85232-R project, from the AEI/FEDER, UE (PID2020-118479RB-I00), and from Generalitat de Catalunya (2017 SGR 1377), is acknowledged. The work of M.M. has been done as a part of the Ph.D. program in Physics at Universitat Autònoma de Barcelona and was financially supported by the Spanish Ministry of Science, Innovation and Universities (BES-2015-075223). A.V. and R.V. acknowledge support by the Deutsche Forschungsgemeinschaft (DFG, German Research Foundation) for funding through TRR 288-422213477 (Project B05). J.S. acknowledges support from Project No. 2017 SGR 579 from AGAUR, Generalitat de Catalunya.

- [1] J. B. Goodenough, *J. Solid State Chem.* **3**, 490 (1971).
- [2] D. B. McWhan, A. Menth, J. P. Remeika, W. F. Brinkman, and T. M. Rice, *Phys. Rev. B* **7**, 1920 (1973).
- [3] J.-H. Park, L. H. Tjeng, A. Tanaka, J. W. Allen, C. T. Chen, P. Metcalf, J. M. Honig, F. M. F. de Groot, and G. A. Sawatzky, *Phys. Rev. B* **61**, 11506 (2000).
- [4] M. W. Haverkort, Z. Hu, A. Tanaka, W. Reichelt, S. V. Streltsov, M. A. Korotin, V. I. Anisimov, H. H. Hsieh, H.-J. Lin, C. T. Chen, D. I. Khomskii, and L. H. Tjeng, *Phys. Rev. Lett.* **95**, 196404 (2005).
- [5] C. F. Hague, J. M. Mariot, V. Ilakovac, R. Delaunay, M. Marsi, M. Sacchi, J.-P. Rueff, and W. Felsch, *Phys. Rev. B* **77**, 045132 (2008).
- [6] M. Abbate, F. M. F. de Groot, J. C. Fuggle, Y. J. Ma, C. T. Chen, F. Sette, A. Fujimori, Y. Ueda, and K. Kosuge, *Phys. Rev. B* **43**, 7263 (1991).
- [7] N. B. Aetukuri, A. X. Gray, M. Drouard, M. Cossale, L. Gao, A. H. Reid, R. Kukreja, H. Ohldag, C. A. Jenkins, E. Arenholz, K. P. Roche, H. A. Dürr, M. G. Samant, and S. S. P. Parkin, *Nat. Phys.* **9**, 661 (2013).
- [8] L. Zhang, Y. Zhou, L. Guo, W. Zhao, A. Barnes, H. T. Zhang, C. Eaton, Y. Zheng, M. Brahlek, H. F. Haneef, N. J. Podraza, M. H. W. Chan, V. Gopalan, K. M. Rabe, and R. Engel-Herbert, *Nat. Mater.* **15**, 204 (2016).
- [9] M. Mirjolet, F. Sánchez, and J. Fontcuberta, *Adv. Funct. Mater.* **29**, 1808432 (2019).
- [10] S. Backes *et al.*, *Phys. Rev. B* **94**, 241110(R) (2016).
- [11] F. Frati, M. O. J. Y. Hunault, and F. M. F. de Groot, *Chem. Rev.* **120**, 4056 (2020).
- [12] F. Iga, M. Tsubota, M. Sawada, H. B. Huang, S. Kura, M. Takemura, K. Yaji, M. Nagira, A. Kimura, T. Jo, T. Takabatake, H. Namatame, and M. Taniguchi, *Phys. Rev. Lett.* **93**, 257207 (2004).
- [13] C. Aruta, G. Ghiringhelli, V. Bisogni, L. Braicovich, N. B. Brookes, A. Tebano, and G. Balestrino, *Phys. Rev. B* **80**, 014431 (2009).
- [14] D. Pesquera, G. Herranz, A. Barla, E. Pellegrin, F. Bondino, E. Magnano, F. Sánchez, and J. Fontcuberta, *Nat. Commun.* **3**, 1189 (2012).
- [15] E. J. Guo, R. D. Desautels, D. Keavney, A. Herklotz, T. Z. Ward, M. R. Fitzsimmons, and H. N. Lee, *Phys. Rev. Mater.* **3**, 014407 (2019).
- [16] J. Chakhalian, J. M. Rondinelli, J. Liu, B. A. Gray, M. Kareev, E. J. Moon, N. Prasai, J. L. Cohn, M. Varela, I. C. Tung, M. J. Bedzyk, S. G. Altendorf, F. Strigari, B. Dabrowski, L. H. Tjeng, P. J. Ryan, and J. W. Freeland, *Phys. Rev. Lett.* **107**, 116805 (2011).
- [17] S. Middey, D. Meyers, S. K. Ojha, M. Kareev, X. Liu, Y. Cao, J. W. Freeland, and J. Chakhalian, *Phys. Rev. B* **98**, 045115 (2018).
- [18] H. B. Vasili, D. Pesquera, M. Valvidares, P. Gargiani, E. Pellegrin, F. Bondino, E. Magnano, A. Barla, and J. Fontcuberta, *Phys. Rev. Mater.* **4**, 044404 (2020).
- [19] J. Chakhalian, J. W. Freeland, H.-U. Habermeier, G. Cristiani, G. Khaliullin, M. Van Veenendaal, and B. Keimer, *Science* **318**, 1114 (2007).
- [20] R. Werner, C. Raisch, A. Ruosi, B. A. Davidson, P. Nagel, M. Merz, S. Schuppler, M. Glaser, J. Fujii, T. Chassé, R. Kleiner, and D. Koelle, *Phys. Rev. B* **82**, 224509 (2010).
- [21] A. Galdi, C. Aruta, P. Orgiani, C. Adamo, V. Bisogni, N. B. Brookes, G. Ghiringhelli, D. G. Schlom, P. Thakur, and L. Maritato, *Phys. Rev. B* **85**, 125129 (2012).
- [22] T. C. Koethe, Z. Hu, M. W. Haverkort, C. Schüßler-Langeheine, F. Venturini, N. B. Brookes, O. Tjernberg, W. Reichelt, H. H. Hsieh, H. J. Lin, C. T. Chen, and L. H. Tjeng, *Phys. Rev. Lett.* **97**, 116402 (2006).
- [23] J. Wang, G. Rijnders, and G. Koster, *Appl. Phys. Lett.* **113**, 223103 (2018).
- [24] See Supplemental Material at <http://link.aps.org/supplemental/10.1103/PhysRevMaterials.5.095002> for (1) surface morphology (S1), (2) additional data on structural characterization (S2), (3) additional data on electrical characterization (S3), (4) XAS/XLD at grazing and normal angles of incidence (S4), (5) temperature dependence of XAS/XLD (S5), (6) thickness dependence of XAS/XLD (S6), (7) angular dependence of the XLD (S7), (8) IDOS calculations for V d orbitals (S8), and (9) charge unbalance among V d and O p orbitals (S9). Also see Refs. [14,18,31,45–49].
- [25] A. Barla, J. Nicolás, D. Cocco, S. M. Valvidares, J. Herrero-Martín, P. Gargiani, J. Moldes, C. Ruget, E. Pellegrin, and S. Ferrer, *J. Synchrotron Radiat.* **23**, 1507 (2016).
- [26] K. Koepf and H. Eschrig, *Phys. Rev. B* **59**, 1743 (1999).
- [27] I. Opahle, K. Koepf, and H. Eschrig, *Phys. Rev. B* **60**, 14035 (1999).
- [28] H. Eschrig, K. Koepf, and I. Chaplygin, *J. Solid State Chem.* **176**, 482 (2003).
- [29] J. A. Moyer, C. Eaton, and R. Engel-Herbert, *Adv. Mater.* **25**, 3578 (2013).
- [30] U. Aschauer, R. Pfenninger, S. M. Selbach, T. Grande, and N. A. Spaldin, *Phys. Rev. B* **88**, 054111 (2013).
- [31] M. Mirjolet, H. B. Vasili, L. López-Conesa, S. Estradé, F. Peiró, J. Santiso, F. Sánchez, P. Machado, P. Gargiani, M. Valvidares, and J. Fontcuberta, *Adv. Funct. Mater.* **29**, 1904238 (2019).
- [32] A. Boileau, A. Cheikh, A. Fouchet, A. David, C. Labbé, P. Marie, F. Gourbilleau, and U. Lüders, *Adv. Opt. Mater.* **7**, 1801516 (2019).
- [33] M. Abbate, H. Pen, M. T. Czyzyk, F. M. F. de Groot, J. C. Fuggle, Y. J. Ma, C. T. Chen, F. Sette, A. Fujimori, Y. Ueda, and K. Kosuge, *J. Electron Spectros. Relat. Phenomena* **62**, 185 (1993).
- [34] D. Maganas, M. Roemelt, T. Weyhermüller, R. Blume, M. Hävecker, A. Knop-Gericke, S. DeBeer, R. Schlögl, and F. Neese, *Phys. Chem. Chem. Phys.* **16**, 264 (2014).
- [35] Q. Lu, S. R. Bishop, D. Lee, S. Lee, H. Bluhm, H. L. Tuller, H. N. Lee, and B. Yildiz, *Adv. Funct. Mater.* **28**, 1803024 (2018).
- [36] M. Wu, J.-C. Zheng, and H.-Q. Wang, *Phys. Rev. B* **97**, 245138 (2018).
- [37] M. Liberati, R. V. Chopdekar, V. Mehta, E. Arenholz, and Y. Suzuki, *J. Magn. Magn. Mater.* **321**, 2852 (2009).
- [38] C. Hébert, M. Willinger, D. S. Su, P. Pongratz, P. Schattschneider, and R. Schlögl, *Eur. Phys. J. B* **28**, 407 (2002).
- [39] A. Gloskovskii, S. A. Nepijko, G. Schönhense, H. A. Therese, A. Reiber, H. C. Kandpal, G. H. Fecher, C. Felser, W. Tremel, and M. Klimenkov, *J. Appl. Phys.* **101**, 084301 (2007).
- [40] F. M. F. de Groot, M. Grioni, J. C. Fuggle, J. Ghijsen, G. A. Sawatzky, and H. Petersen, *Phys. Rev. B* **40**, 5715 (1989).

- [41] C. C. Ahn, O. L. Krivanek, and M. M. Disko, *EELS Atlas: A Reference Guide of Electron Energy Loss Spectra Covering All Stable Elements*, HREM Facility, Center for Solid State Science, Arizona State University (1983).
- [42] D. S. Su, H. W. Zandbergen, P. C. Tiemeijer, G. Kothleitner, M. Hävecker, C. Hébert, A. Knop-Gericke, B. H. Freitag, F. Hofer, and R. Schlögl, *Micron* **34**, 235 (2003).
- [43] M. G. Brik, K. Ogasawara, H. Ikeno, and I. Tanaka, *Eur. Phys. J. B* **51**, 345 (2006).
- [44] J. G. Chen, *Surf. Sci. Rep.* **30**, 1 (1997).
- [45] S. Pandya, A. R. Damodaran, R. Xu, S.-L. Hsu, J. C. Agar, and L. W. Martin, *Sci. Rep.* **6**, 26075 (2016).
- [46] F. Sánchez, I. C. Infante, U. Lüders, L. Abad, and J. Fontcuberta, *Surf. Sci.* **600**, 1231 (2006).
- [47] M. Kalf, P. Šmilauer, G. Comsa, and T. Michely, *Surf. Sci.* **426**, L447 (1999).
- [48] G. Ehrlich and F. G. Hudda, *J. Chem. Phys.* **44**, 1039 (1966).
- [49] R. L. Schwoebel and E. J. Shipsey, *J. Appl. Phys.* **37**, 3682 (1966).